

Crystal phase engineering $\text{Zn}_{0.8}\text{Cd}_{0.2}\text{S}$ nanocrystals with twin-induced homojunctions for photocatalytic nitrogen fixation under visible light

Wanyue Dong^{a,b}, Yutang Liu^{a,b,*}, Guangming Zeng^{a,b}, Tao Cai^{a,b}, Luhua Shao^c, Hui Chen^{a,b}, Wengao Zeng^{a,b}, Xinnian Xia^a

^a College of Environmental Science and Engineering, Hunan University, Lushan South Road, Yuelu District, Changsha 410082, PR China

^b Key Laboratory of Environmental Biology and Pollution Control (Hunan University), Ministry of Education, Lushan South Road, Yuelu District, Changsha 410082, PR China

^c College of Chemistry and Chemical Engineering, Hunan University, Changsha 410082, PR China

ARTICLE INFO

Keywords:

Photocatalysis
Nitrogen fixation
Twinned $\text{Zn}_{0.8}\text{Cd}_{0.2}\text{S}$
Homojunction

ABSTRACT

Newly developed photocatalysts usually focus on structuring active sites, for enhancing chemical adsorption and reducing activation energy barrier in photocatalysis nitrogen fixation. However, lots of photocatalysts suffer from electron-hole pairs' recombination in the bulk or on the surface during transportation. Herein, twinned $\text{Zn}_{0.8}\text{Cd}_{0.2}\text{S}$ nanocrystals were successfully applied to photocatalytic nitrogen fixation, affording an ammonia production rate of $66.91 \mu\text{mol g}^{-1} \text{h}^{-1}$ under visible light with an AQE of 3.77 % at 420 nm, which were 17-fold and 3-fold higher than the activities of CdS and ZnS, respectively. The inner homojunction enhanced carriers' transportation, and improved electrons density on zinc blend segment, which could facilitate adsorption of nitrogen and $\cdot\text{H}$ gaining, finally, the nitrogen activation and reduction proceeded through the six electrons reduction process on (111) facets. These results confirm that twinned $\text{Zn}_{0.8}\text{Cd}_{0.2}\text{S}$ nanocrystal is a kind of promising new photocatalyst for solar-driven nitrogen reduction to ammonia.

1. Introduction

Ammonia is a substantial commodity chemical that is increasingly prevalent in the industry for the production of pharmaceuticals, fertilizers, polymers, and various other consumer products. In addition, NH_3 can be used as a fuel or H_2 carrier [1].

During the traditional Haber-Bosch process for artificial nitrogen (N_2) fixation, it is necessary to input extra high temperature and pressure to overcome the extremely strong triple bond and the kinetic inertness of N_2 and to ensure the reaction efficiency [2]. Different from Haber-Bosch process, the FeMo-based nitrogenase possesses the function to bind N_2 and weaken the triple bond under mild conditions in nature, thus to prompt subsequent electrons transfer and protons attack [3,4].

Enlightened by biological N_2 fixation under ambient conditions, newly developed photocatalytic N_2 fixation methods have been proposed recently [5]. Most investigations focus on structuring active sites on photocatalysts, such as vacancy creation, heteroatom doping, surface modification, and composite construction, etc, to accumulate electrons, optimize reactant chemical adsorption and reduce activation energy barriers [6]. Crystal phase engineering is a method to

directionally distribute photo-generated current carriers, which can significantly change the properties of photocatalysts.

$\text{Zn}_{1-x}\text{Cd}_x\text{S}$ solid solutions are a type of pseudobinary sulfide with tunable band gaps and preferable stability [7]. Induced by alkaline complexant, zinc blend (ZB) and wurtzite (WZ) phases can coexist in a single $\text{Zn}_{1-x}\text{Cd}_x\text{S}$ nanocrystal (NC). Moreover, homojunctions between two different crystal phases can enhance the separation of electron-hole pairs and steer their transport pathways, thus preventing the recombination. The distribution density of homojunctions can also be tuned by regulating the value of x. By virtue of coordinating band structure and crystal phase structure, photocatalysts are bestowed with superior carrier separation function and appropriate reaction potential, thus being able to satisfy various reaction requirements.

Herein, we creatively reported the activity and mechanism of photocatalytic N_2 reduction to NH_3 by twinning $\text{Zn}_{0.8}\text{Cd}_{0.2}\text{S}$ nanocrystals (NCs). Specifically, under visible light ($\lambda \geq 420 \text{ nm}$), we have achieved a photocatalytic NH_3 production rate of $66.91 \mu\text{mol g}^{-1} \text{h}^{-1}$ and an apparent quantum efficiency (AQE) of 3.77 % at 420 nm, about 17-fold and 3-fold higher than those of pristine CdS and ZnS, respectively. $\text{Zn}_{0.8}\text{Cd}_{0.2}\text{S}$ NCs were capable of providing sufficient electrons for every step involved in the reduction of N_2 to NH_3 , the band structure of

* Corresponding author at: College of Environmental Science and Engineering, Hunan University, Lushan South Road, Yuelu District, Changsha 410082, PR China.
E-mail address: yt_liu@hnu.edu.cn (Y. Liu).

Zn_{0.8}Cd_{0.2}S NCs satisfied the six-electron transfer reaction potential, and the inner homojunctions could provide active charge kinetics [8]. As demonstrated that with crystalline phase engineering, it is possible to purposefully design photocatalysts for particular reactions in energy and environmental applications [9].

2. Experimental

2.1. Chemical

All chemicals used in this work were described in Supplementary information (SI Text S1).

2.2. Photocatalyst synthesis

The Zn_{1-x}Cd_xS photocatalysts were synthesized according to our previously reported method (SI Text S1) [10,11].

2.3. Characterizations

The crystal structures were determined by X-ray diffraction (XRD) with 40 kV/30 mA Cu-K α radiation (LabX XRD-6100, Shimadzu, Japan). The chemical composition characterization was operated by X-ray photoelectron spectroscopy (XPS) with Al-K α radiation (Thermo Fisher Scientific, England). The morphologies were observed with field emission scanning electron microscopy (FE-SEM) (S-4800, Hitachi, Japan) and transmittance electron microscopy (TEM) (JEM-2100 F, JEOL, Japan).

2.4. Photoelectrochemical tests

The UV-vis diffuse reflectance spectra (DRS) of the samples were obtained with a UV-vis spectrophotometer (UV2550, Shimadzu, Japan). The photoelectrochemical tests were carried out on the CS310H electrochemical workstation with the standard three-electrodes mode, and 0.1 M Na₂SO₄ aqueous solution was employed as the electrolyte. The working electrodes were prepared as described below: 5 mg of the Zn_xCd_{1-x}S sample was put into a 100 μ L mixture of 950 μ L ethanol and 50 μ L 1% Nafion under ultrasonic dispersion treatment for 30 min. to obtain a uniform suspension, where the Nafion was chosen as the film-forming agent. Then, the suspension was coated onto pieces of fluorine-doped tin oxide (FTO) glass (coating area is about 1 \times 3 cm² each piece) and dried for 4 h at 80°C in drying oven. The Ag/AgCl electrode and platinum wire were utilized as the reference electrode and counter electrode, respectively. The transient photocurrent response measurement was performed by turning on or off the light. A 300 W xenon lamp was used as a light source. The electrochemical impedance spectroscopy (EIS) was collected with an amplitude of 0.005 V over the frequency that ranges from 1 to 10⁵ Hz, and Mott-Schottky curves were also recorded at the frequency of 1000 Hz and 1200 Hz. The photoluminescence (PL) spectra were recorded on a Hitachi F-7000 fluorescence spectrophotometer with the excitation wavelength of 325 nm, scanning speed of 1200 nm/min, and PMT voltage of 700 V. Time-resolved photoluminescence (TRPL) spectra were collected on an FS5 fluorescence spectrophotometer (Edinburgh Instruments, UK), with excitation wavelength at 420 nm.

2.5. Photocatalytic N₂ fixation

The photocatalytic N₂ fixation experiments were carried out under visible light irradiation (λ > 420 nm) using a Xe lamp (PLS-SXE 300C, Beijing Perfect Light Co., Ltd., China) as the light source. 25 mg photocatalyst was added to Pyrex photocatalytic reactor containing 50 mL of distilled water or 1 mM Na₂SO₃ aqueous solution, in which Na₂SO₃ was used as a hole sacrificial agent. Before light irradiation, the mixture solution was constantly stirred in the dark with high-purity N₂ bubbled

at a flow rate of 60 mL/min for 30 min. The experiment temperature was stabilized at 20°C using a circulating water system. At certain time intervals, NH₃ concentration was determined by the color reagent mentioned below.

2.6. Determination of NH₃ production

The salicylic acid analysis method was utilized to determine NH₃ concentration by UV-vis spectrophotometry [12–14]. Detailed steps were described as follows, 4 mL solution was removed from the reaction vessel and mixed with 50 μ L oxidizing solution consisting of NaClO (Effective chlorine \geq 5.0 %) and NaOH (0.75 M), 500 μ L coloring solution containing 0.4 M C₇H₆O₃ and 0.7 M NaOH and 50 μ L catalyst solution (Na₂[Fe(CN)₅NO]·2H₂O solution with a concentration of 10 mg mL⁻¹) in turn.

The concentration-absorbance standard curve was calibrated using standard NH₄Cl solution with NH₃ concentrations of 0, 0.1, 0.2, 0.3, 0.4, 0.5, 0.6, 0.7, 0.8, 0.9, and 1.0 μ g·mL⁻¹ in distilled water. As the concentration of NH₃ increases, the standard NH₄Cl solution appeared ordered the colour change from yellow to green. (inserted in Fig. S1A) As shown in Fig. S1A, the calibration curve (Fitting equation $y = 0.02205 + 0.2591x$, $R^2 > 0.999$) was used to calculate the NH₃ concentration. Absorbance measurements were performed after 4 h at $\lambda = 660$ nm. (Fig. S1B)

The apparent quantum efficiency (AQE) calculation was stated in Text S2.

3. Result and discussion

3.1. Structure and morphology characterization

In Fig. 1A, the characteristic diffraction peaks of ZnS with ZB structure and CdS with WZ structure were calibrated sequentially. After part of Zn²⁺ replaced by Cd²⁺, the diffraction peaks of Zn_{0.8}Cd_{0.2}S arose at $2\theta = 28.52^\circ, 33.02^\circ, 47.52^\circ, 56.34^\circ$ correspond to the (111), (200), (220), (311) facets of ZnS in turn. In the meantime, the intensity of these peaks above gets weakened compared to ZnS, revealing the reduced crystal purity, and lower exposure degree of corresponding crystal facets [15]. On the other hand, tiny diffraction peaks appeared at lower angle $2\theta = 28.06^\circ, 46.38^\circ, 55.22^\circ$ near the major peaks, for small-angle shift usually means doping of heteroatoms with larger radius. In Fig. 1B, the regional XRD spectra of Zn_{1-x}Cd_xS samples (full spectra in Fig. S2), the main diffraction peaks showed gradually shift along with the Cd²⁺ doping quantity (x), indicating different degrees of crystalline phase mixing [16–18]. The average crystallite sizes of ZnS, Zn_{0.8}Cd_{0.2}S, and CdS was calculated by the Scherrer formula in Table S1 and depicted in SEM images (Fig. S3). The smaller crystallite size of Zn_{0.8}Cd_{0.2}S could attribute to its mixed-phase structure, which might inhibit crystal growth [19].

STEM, elemental mapping images and energy dispersive spectrometry (EDS) analysis were employed to further confirm the formation of Zn_{0.8}Cd_{0.2}S solid solution, rather than physical mixing of ZnS and CdS. As depicted in Fig. 2A, the uniformly dispersed Cd, Zn, S elements possess different densities, corresponding to the EDS spectrum intensity and the atomic ratio of Zn_{0.8}Cd_{0.2}S in Fig. 2B and Table S2, and consistent with the inputs of raw material. The XPS survey spectrum (Fig. S4) also confirmed the coexistence of Zn, Cd, and S elements, which implied the successful synthesis of a solid solution. High-resolution XPS signals of Cd 3d_{5/2} and Cd 3d_{3/2} appear at approximately 404.09 eV and 410.79 eV, respectively, while those of Zn 2p_{3/2} and Zn 2p_{1/2} are centered at around 1021.09 eV and 1043.89 eV, respectively. The S 2p single peak arises at 160.89 eV indicates the existence of the sulfur ions [20]. With a slightly shifting, XPS of the as-prepared sample basically in accordance with previous studies [10,11,21–23].

The anisotropic Zn_{0.8}Cd_{0.2}S NCs with chrysalis-like morphology can be seen in the TEM image (Fig. 2C). For a single particle, on the

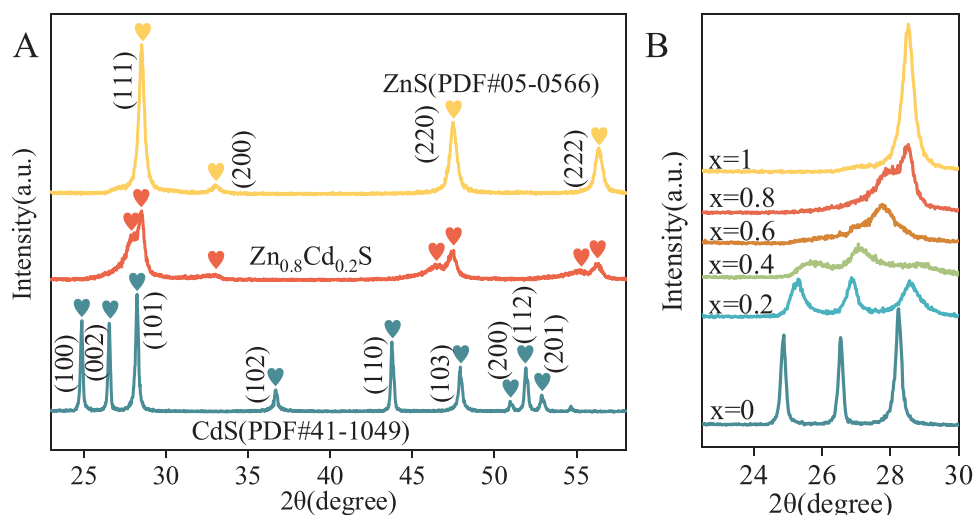


Fig. 1. XRD patterns of CdS, ZnS and $Zn_{0.8}Cd_{0.2}S$ NCs (A); magnification XRD patterns of $Zn_xCd_{1-x}S$ solid solutions in region 22° - 30° (B).

unsmooth surface of the particles, relatively high density of strip-like stacking faults distribute in parallel, shown in the inset of Fig. 2D. As depicted in HRTEM image (Fig. 2D), these dislocations have made up coherent twin boundaries, by suddenly destroying the lattice continuity and simultaneously introducing WZ segments at intervals among major ZB segments, and then formed a series of twin-induced homojunctions. The measured lattice spacing was about 0.33 nm, which can be ascribed to the (111) crystal planes of $Zn_{0.8}Cd_{0.2}S$. In Fig. 2E, the SAED pattern also evinced the nano-twin structure of $Zn_{0.8}Cd_{0.2}S$ NCs. There are two sets of diffraction spots arrange in parallelograms sharing common vertices, being regarded as the diffraction feature of the twinning structure, which indicated both ZB and WZ phases in $Zn_{0.8}Cd_{0.2}S$ NCs [24–26].

3.2. Band gap structure

Fig. 3A depicts UV-vis DRS of the ZnS, $Zn_{0.8}Cd_{0.2}S$, and CdS. The absorption edge of ZnS at about 350 nm, signifying the wide band gap. Partly, by altering the Zn/Cd atomic ration, band gap of $Zn_{1-x}Cd_xS$ solid solution could be tuned to a certain value. (Fig. S5) As the Cd^{2+} nominal content increase, the absorption edge of $Zn_{0.8}Cd_{0.2}S$ showed obviously redshifts to 520 nm and presented elevated visible light absorption in the meantime [27]. The band gap energy (E_g) of them was calculated by Kubelka-Munk method in Fig. 3B, which extrapolate the linear plots of the Kubelka-Munk function $(F(R)h\nu)^2$ vs. exciting light energy ($h\nu$) to $F(R) = 0$, the E_g of ZnS, $Zn_{0.8}Cd_{0.2}S$, and CdS were 3.60 eV, 2.64 eV, 2.40 eV, respectively [28,29]. The Mott-Schottky (MS) plots were recorded to estimate the p-n type nature of semiconductors and flat band potential (E_{fb}). As shown in Fig. 3C–E, the positive slopes

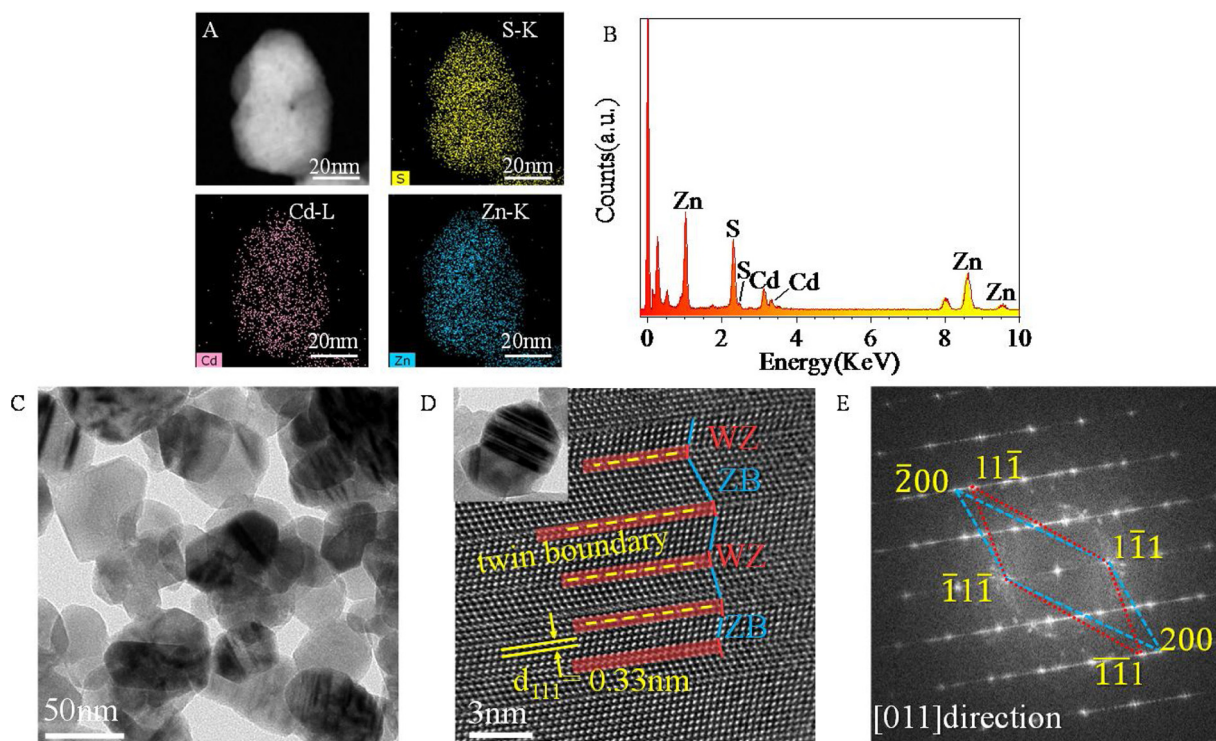


Fig. 2. STEM image, element mapping images (A) and EDS spectrum (B) of a single $Zn_{0.8}Cd_{0.2}S$ NC; TEM images of the $Zn_{0.8}Cd_{0.2}S$ NCs (C), high density of twin planes on $Zn_{0.8}Cd_{0.2}S$ NC (inset in D), corresponding HRTEM image of ZB/WZ homojunction with zigzag structure (D) and the SAED pattern (E).

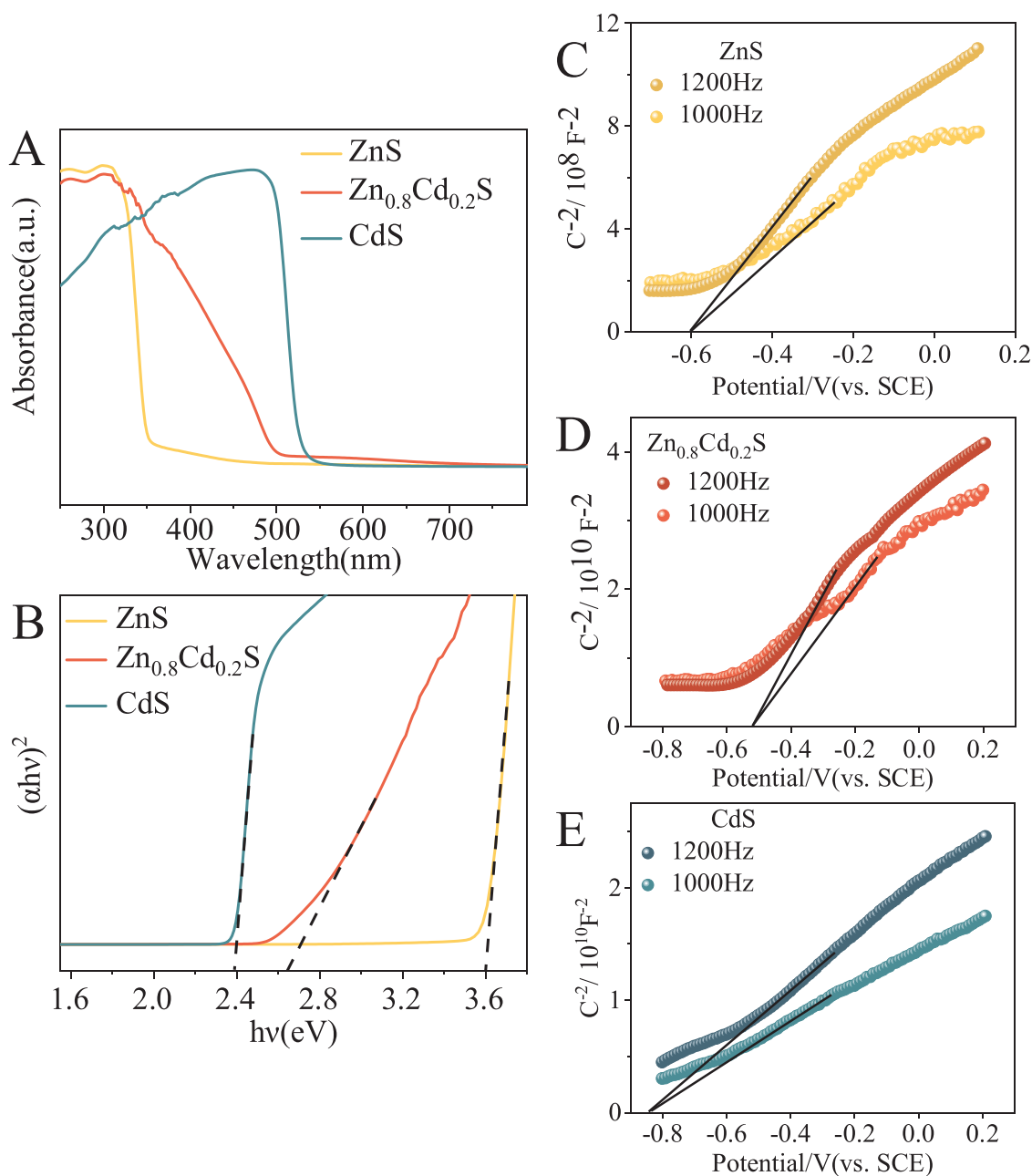


Fig. 3. UV-vis DRS (A) and Kubelka-Munk plots (B) of band gap energies for ZnS, Zn_{0.8}Cd_{0.2}S and CdS NCs and corresponding Mott-Schottky plots (C-E).

indicate that all the samples were of n-type. Based on MS equation, E_{fb} of ZnS, Zn_{0.8}Cd_{0.2}S, and CdS can be estimated to be -0.60 V, -0.52 V, and -0.83 V vs SCE, equal to -0.40 V, -0.32 V, and -0.63 V vs NHE, respectively. Generally, the CB of n-type semiconductors would be 0~0.2 V more negative than the E_{fb} , hence the CB of ZnS, Zn_{0.8}Cd_{0.2}S, and CdS could be regarded as -0.60 V, -0.52 V and -0.83 V vs NHE, respectively [28,30–34]. Combined with the DRS band gap energy estimation, the band gap structure of samples was depicted in Fig. 6, and detailed data was in Table S3.

3.3. Evaluation of photocatalytic activity

The photocatalytic activities of Zn_{1-x}Cd_xS NCs were evaluated by photocatalytic N₂ fixation, the yield NH₃ was measured according to the standard curve of NH₃ (Fig. S1). Zn_{0.8}Cd_{0.2}S has shown the best photocatalytic N₂ fixation activity in 2 h among a series of Zn_{1-x}Cd_xS, as shown in Fig. 4A and Table S4. Fig. 4B compares the NH₃ production of

Zn_{0.8}Cd_{0.2}S under different conditions. With addition of the hole sacrificial agent Na₂SO₃, the photocatalytic N₂ fixation activity of Zn_{0.8}Cd_{0.2}S was obviously raised than it in pure H₂O. While with addition of the electron sacrificial agent KBrO₃, the photocatalytic N₂ fixation activity decreased. These photocatalytic activity changes were attributed to the change of electrons' concentration, when a part of holes be consumed by Na₂SO₃, the separation of photo-generated carriers is facilitated, and the activity decrease with the addition of KBrO₃ suggesting the role of electrons in photocatalytic N₂ fixation reaction. NH₃ was scarcely detected in the absence of catalyst, but a little amount of NH₃ was detected with the catalyst under dark condition, it may come from the amino-containing complexants during the synthesizing process. The control experiment (N₂ replaced by Ar) revealed that with longer irradiation time (Fig. S6), the trace amount of NH₃ didn't obviously increase, confirming that most of the NH₃ produced come from N₂ photofixation [35–37]. Fig. 4C and Table S5 have shown the comparison for photocatalytic N₂ fixation activity of ZnS, Zn_{0.8}Cd_{0.2}S and,

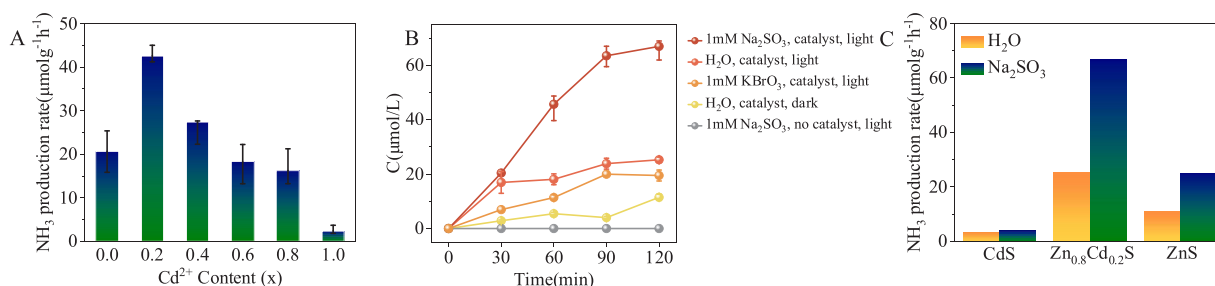


Fig. 4. NH₃ production rate of Zn_{1-x}Cd_xS samples under visible light in 2 h, Na₂SO₃ as a sacrificial agent (A); controlled experiments of Zn_{0.8}Cd_{0.2}S on photocatalytic NH₃ production (B); photocatalytic N₂ fixation activity comparison between CdS, Zn_{0.8}Cd_{0.2}S, ZnS (C).

CdS with or without the sacrificial agent, Fig. S7 and Table S6 also depicted the obtained NH₃ concentration overtime for them. Zn_{0.8}Cd_{0.2}S achieved an NH₃ production rate of 66.91 μmol g⁻¹ h⁻¹ under visible light, which was about 17-fold higher than that of CdS (4.01 μmol g⁻¹ h⁻¹) and 3-fold higher than that of ZnS (24.98 μmol g⁻¹ h⁻¹), proving the role of homojunction in photocatalytic N₂ fixation. The photocatalytic stability of Zn_{0.8}Cd_{0.2}S was verified over morphology and phase structure characteristics before and after the reaction, as well as the NH₃ production performance (Fig. S8). Table S7 compares the performance of current N₂ photo-fixation systems, it is considered that Zn_{0.8}Cd_{0.2}S can be a relatively efficient photocatalyst.

3.4. Charge transfer properties

EIS Nyquist plot is a method to elucidate the charge transfer behavior, and a smaller arc radius usually indicates less charge transfer resistance [38]. As disclosed in Fig. 5A and S9, the always smallest arc radius of Zn_{0.8}Cd_{0.2}S with or without light irradiation, suggested the lowest inner transfer resistance of boosted electron in twinning NCs

semiconductor [7,39]. Fig. 5B reflects the transient photocurrent responses of the samples under visible light irradiation. As expected, Zn_{0.8}Cd_{0.2}S showed a much higher photocurrent compared to that of ZnS and CdS, indicating that Zn_{0.8}Cd_{0.2}S possesses the quickest separation performance of photo-excited charges [40]. Time-resolved photoluminescence (TRPL) measurement and steady-state photoluminescence (PL) technique were also performed on ZnS, Zn_{0.8}Cd_{0.2}S, and CdS to illustrate the separation and recombination of photo-generated carriers, as displayed in Fig. 5C and D. For TRPL, each component's emission lifetimes and corresponding amplitudes were listed in Table S9, along with the biexponential (triexponential for ZnS) fitting equation for decay spectra in Fig. 5C and average lifetime calculation equation. Thus, TRPL spectroscopy revealed the PL lifetime of 0.63 ns for Zn_{0.8}Cd_{0.2}S, which was shorter than that of ZnS (1.74 ns) and CdS (0.67 ns). The pure ZB phase ZnS exhibits three lifetimes, the longest component τ_3 is attributed to localized exciton recombination, as the photo-generated carriers in deep bulk ZnS nanocrystals cannot diffuse successfully to the surface, thus normally long-lived and less be quenched. Besides band gaps, the crystal sizes of CdS and Zn_{0.8}Cd_{0.2}S were

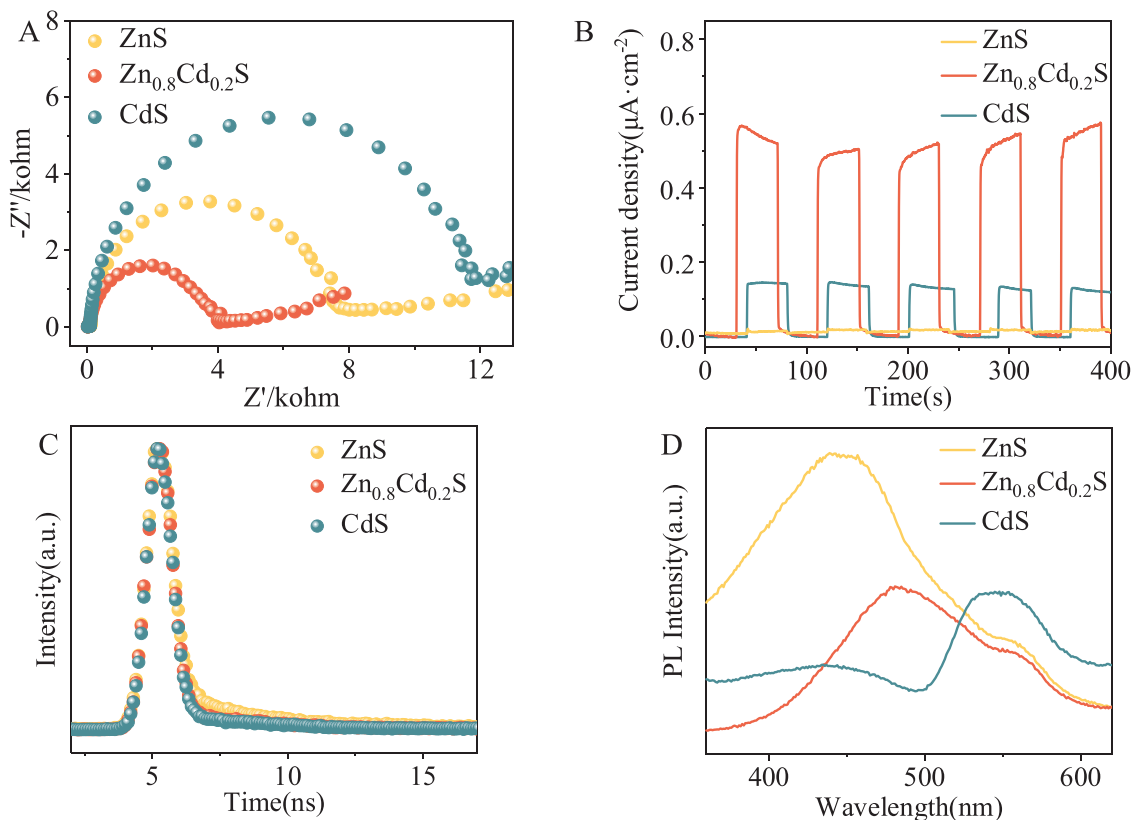


Fig. 5. Nyquist impedance plots (A), transient photocurrent responses (B) time-resolved photoluminescence decay spectra (C) and steady-state photoluminescence spectra (D) of ZnS, Zn_{0.8}Cd_{0.2}S and CdS NCs.

also smaller than ZnS, and most photo-generated carriers were consumed by H₂O molecules, thus component τ_3 disappeared. The τ_1 and τ_2 of Zn_{0.8}Cd_{0.2}S were both longer than CdS, however, due to the special atom arrangement of Zn_{0.8}Cd_{0.2}S, the amplitude B1 of τ_1 increased, indicating the carriers transport was directed by the ZB/WZ homojunction and more on the surface. The shorter PL lifetime of Zn_{0.8}Cd_{0.2}S could be attributed to the delocalization of excitons within Zn_{0.8}Cd_{0.2}S being improved, and thereby contributing more non-radiative recombination of these excitons, leading to a reduction of the PL lifetime [41–43]. As exhibited in Fig. 5D, with the increase of Cd content, PL emission peak of Zn_{0.8}Cd_{0.2}S exhibited obvious red-shift and intensity decline compared to that of ZnS [10]. These photoelectrochemical tests above both indicated that under visible light, electrons' excitation and transportation in Zn_{0.8}Cd_{0.2}S are much effective than barely in either ZnS or CdS, with their enhanced separation, extended lifetime and orderly migration. This is due to the function of inner homojunctions in the single Zn_{0.8}Cd_{0.2}S solid solution semiconductor.

3.5. Photocatalytic N₂ fixation mechanism

Based on the above results, the enhancement of nitrogen fixation activity on Zn_{0.8}Cd_{0.2}S can be explained with Fig. 6A, the CB potentials of all samples were both more negative than six electrons transfer reaction potential, as Eq. (1) [21,44].



The nitrogen fixation activity of ZnS could be ascribed to the surface defects, which would be excited under visible light irradiation and generate free electrons. However, from the viewpoint of thermodynamics, the relatively wide band gap of ZnS increases the opportunity of electron-hole pairs' recombination. Moreover, CdS usually suffer from photocorrosion for holes that could oxidize its own S²⁻ to S and/or sulfate (SO₄²⁻), thus, its photocatalytic activity would sharply drop under a long-time photo-irradiation. As vacancies of photocatalysts

were commonly regarded as a kind of active sites for N₂ fixation, for the localized electrons on surface vacancies usually assists the adsorption of inert gas molecules. The ESR signal exhibited at a g value of 2.003 is assigned to SVs (Fig. S10), thus, the N₂ adsorption on Zn_{0.8}Cd_{0.2}S is evidential. Other than band gap energy and surface vacancies, the mixed crystal structure of Zn_{0.8}Cd_{0.2}S is relevant to its better performance. As the stacking fault happens within Zn_{0.8}Cd_{0.2}S solid solution, the atomic arrangement sequence "ABCABCA..." along the <111> direction of pure ZB phase would be broken, inserting WZ sequence "CACAC..." into it at the interval, get the symmetry "ABCACBA..." sequence finally. The middle atomic layer A represents the twin boundary. The interval twinning constitutes mini-bands in which both CB and VB potential are slightly higher than that of bulk ZB phase, thus forms the type-II ZB/WZ homojunction, which could transfer carriers directionally and converge electrons to ZB segment. With higher local density, captive electrons of Zn_{0.8}Cd_{0.2}S were able to effectively participate in the process of N₂ adsorption and ·H gaining, as illustrate in scheme Fig. 6B. According to XRD and lattice spacing determination, the (111) facets were most exposed in ZB segment, thus, corresponding adsorption models (Fig. S11) and adsorption energy calculation (Table S9) was set on (111) crystal facets of Zn_{0.8}Cd_{0.2}S. In the meantime, the holes were gathered on the VB of segments of WZ, away from the reduction site, and partly consumed by the sacrificial reagents (S²⁻ and SO₃²⁻). Finally, the photo-induced carrier separation was highly improved, the electrons then get increased.

4. Conclusions

In summary, we have developed a Zn_{0.8}Cd_{0.2}S solid solution photocatalyst with twin structure for photocatalytic N₂ fixation to NH₃. The coexisting major zinc blende and minor wurtzite phases were the constitutions of homojunctions in twinning Zn_{0.8}Cd_{0.2}S nanocrystals. Zn_{0.8}Cd_{0.2}S has achieved optimal photocatalytic nitrogen fixation efficiency among a series of Zn_xCd_{1-x}S solid solution NC samples.

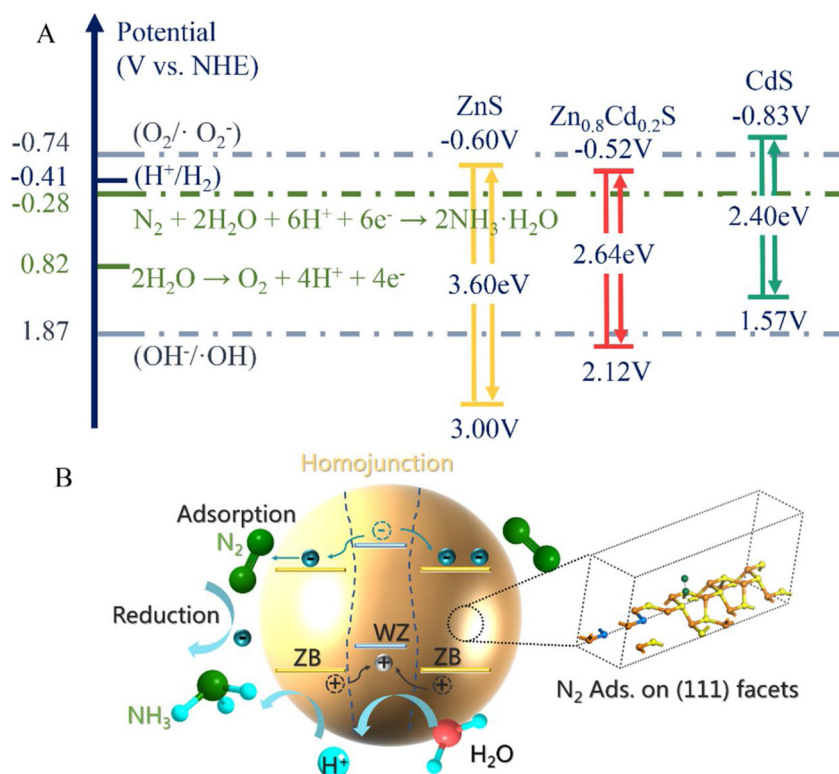


Fig. 6. Relevant reaction potentials and band structures of ZnS, Zn_{0.8}Cd_{0.2}S and CdS NCs (A) and proposed mechanism illustration of the photocatalytic N₂ fixation over homojunction in Zn_{0.8}Cd_{0.2}S twinning NCs photocatalyst (B).

Photoelectrochemical test results demonstrated the intensified electrons' excitation, directional charge carriers' transportation, and tuned appropriate band structure, have improved sufficient electronic supply during N_2 fixation to NH_3 . The (111) crystal facets of ZB segments were inferred to be the main reaction position. Through crystal phase engineering, adjustment of the atom arrangement modes in $Zn_xCd_{1-x}S$ solid solution could provide some new ideas for developing functional novel photocatalysts toward environment and energy utilization.

CRedit authorship contribution statement

Wanyue Dong: Conceptualization, Methodology, Data curation, Writing - original draft. **Yutang Liu:** Supervision, Project administration, Funding acquisition, Writing - review & editing. **Tao Cai:** Validation, Data curation. **Luhua Shao:** Theoretical calculation. **Hui Chen:** Validation, Data curation. **Wengao Zeng:** Formal analysis.

Declaration of Competing Interest

We declare that they have no known competing financial interests or personal relationships that could have appeared to influence the work reported in this paper.

Acknowledgements

This work was supported by the National Natural Science Foundation of China (51521006, 51872089 and 51672077), the Hunan Provincial Natural Science Foundation of China (2017JJ2026) and the Key Laboratory of Jiangxi Province for Persistent Pollutants Control and resources Recycle (Nanchang hangkong University) (ES201880051). The authors thank National supercomputing center in changsha for supporting this work.

Appendix A. Supplementary data

Supplementary material related to this article can be found, in the online version, at doi:<https://doi.org/10.1016/j.jphotochem.2020.112766>.

References

- J. Wang, L. Yu, L. Hu, G. Chen, H. Xin, X. Feng, Ambient ammonia synthesis via palladium-catalyzed electrohydrogenation of dinitrogen at low overpotential, *Nat. Commun.* 9 (2018) 1795.
- H. Li, J. Shang, J. Shi, K. Zhao, L. Zhang, Facet-dependent solar ammonia synthesis of BiOCl nanosheets via a proton-assisted electron transfer pathway, *Nanoscale* 8 (2016) 1986–1993.
- S.C. Lee, R.H. Holm, The clusters of nitrogenase: Synthetic methodology in the construction of weak-field clusters, *Chem. Rev.* 104 (2004) 1135–1158.
- K.A. Brown, D.F. Harris, M.B. Wilker, A. Rasmussen, N. Khadka, H. Hamby, S. Keable, G. Dukovic, J.W. Peters, J.W. Peters, L.C. Seefeldt, P.W. King, Light-driven dinitrogen reduction catalyzed by a Cds: nitrogenase MoFe protein biohybrid, *Science* 352 (2016) 448–450.
- X. Yan, D. Liu, H. Cao, F. Hou, J. Liang, S.X. Dou, Nitrogen reduction to Ammonia on atomic-scale active sites under mild conditions, *Small Methods* (2019).
- Y. Zhao, Y. Zhao, R. Shi, B. Wang, G.I.N. Waterhouse, L.Z. Wu, C.H. Tung, T. Zhang, Tuning oxygen vacancies in ultrathin TiO_2 nanosheets to boost photocatalytic nitrogen fixation up to 700 nm, *Adv. Mater.* 31 (2019) e1806482.
- B.J. Ng, L.K. Putri, X.Y. Kong, K.P.Y. Shak, P. Pasbakhsh, S.P. Chai, A.R. Mohamed, Sub-2 nm Pt-decorated $Zn_{0.5}Cd_{0.5}S$ nanocrystals with twin-induced homojunctions for efficient visible-light-driven photocatalytic H_2 evolution, *Appl. Catal. B* 224 (2018) 360–367.
- S. Bai, J. Jiang, Q. Zhang, Y. Xiong, Steering charge kinetics in photocatalysis: inter-connection of materials syntheses, characterization techniques and theoretical simulations, *Chem. Soc. Rev.* 44 (2015) 2893–2939.
- S. Bai, C. Gao, J.X. Low, Y.J. Xiong, Crystal phase engineering on photocatalytic materials for energy and environmental applications, *Nano Res.* (2018) 1–24.
- H. Du, K. Liang, C.Z. Yuan, H.L. Guo, X. Zhou, Y.F. Jiang, A.W. Xu, Bare $Cd_{1-x}Zn_xS$ ZB/WZ heterophase nanojunctions for visible light photocatalytic hydrogen production with high efficiency, *ACS Appl. Mater. Interfaces* 8 (2016) 24550–24558.
- W. Dong, Y. Liu, G. Zeng, S. Zhang, T. Cai, J. Yuan, H. Chen, J. Gao, C. Liu, Regionalized and vectorial charges transferring of $Cd_{1-x}Zn_xS$ twin nanocrystal homojunctions for visible-light driven photocatalytic applications, *J. Colloid Interface Sci.* 518 (2018) 156–164.
- L. Zhang, X. Ji, X. Ren, Y. Ma, X. Shi, Z. Tian, A.M. Asiri, L. Chen, B. Tang, X. Sun, Electrochemical ammonia synthesis via nitrogen reduction reaction on a MoS_2 catalyst: theoretical and experimental studies, *Adv. Mater.* 30 (2018) e1800191.
- S. Chen, S. Perathoner, C. Ampelli, C. Mebrahtu, D. Su, G. Centi, Electrochemical synthesis of ammonia at room temperature and atmospheric pressure from water and nitrogen on a carbon-nanotube-based electrocatalyst, *Angew. Chem. Int. Ed. Engl.* 56 (2017) 2699–2703.
- D. Yang, T. Chen, Z. Wang, Electrochemical reduction of aqueous nitrogen (N_2) at a low overpotential on (110)-oriented Mo nanofilm, *J. Mater. Chem. A* 5 (2017) 18967–18971.
- Y. Bi, S. Ouyang, N. Umezawa, J. Cao, J.H. Ye, Facet effect of single-crystalline Ag_3PO_4 sub-microcrystals on photocatalytic properties, *J. Am. Chem. Soc.* 133 (2011) 6490–6492.
- W. Li, D. Li, W. Zhang, Y. Hu, Y. He, X. Fu, Microwave synthesis of $Zn_xCd_{1-x}S$ nanorods and their photocatalytic activity under visible light, *J. Phys. Chem. C* 114 (2010) 2154–2159.
- I. Tsuji, H. Kato, H. Kobayashi, A. Kudo, Photocatalytic H_2 evolution reaction from aqueous solutions over band structure-controlled $(Ag)_x(Zn)_{2(1-x)}S_2$ solid solution photocatalysts with visible-light response and their surface nanostructures, *J. Am. Chem. Soc.* 126 (2004) 13406–13413.
- V. Kumar, V. Singh, S.K. Sharma, T.P. Sharma, Structural and optical properties of sintered $Cd_{1-x}Zn_xS$ films, *Opt. Mater.* 11 (1998) 29–34.
- Y.H. Lu, P.X. Wu, J.Y. Huang, L. Tran, N.W. Zhu, Z. Dang, Alkaline-assisted hydrothermal fabrication of CdZnS with enhanced visible-light photocatalytic performance, *Chem. J. Chin. Univ.* 36 (2015) 1563–1569.
- T. Vdovenkov, A. Vdovenkov, R. Tornqvist, ZnS wide band gap semiconductor thin film electronic structure sensitivity to Mn impurity, *Thin Solid Films* 343 (1999) 332–334.
- L. Ye, C. Han, Z. Ma, Y. Leng, J. Li, X. Ji, D. Bi, H. Xie, Z. Huang, Ni_2P loading on $Cd_{0.5}Zn_{0.5}S$ solid solution for exceptional photocatalytic nitrogen fixation under visible light, *Chem. Eng. J.* 307 (2017) 311–318.
- C.C. Shen, Y.N. Liu, X. Zhou, H.L. Guo, Z.W. Zhao, K. Liang, A.W. Xu, Large improvement of visible-light photocatalytic H_2 -evolution based on cocatalyst-free $Zn_{0.5}Cd_{0.5}S$ synthesized through a two-step process, *Catal. Sci. Technol.* 7 (2017) 961–967.
- F.Y. Tian, D. Hou, F. Tang, M. Deng, X.Q. Qiao, Q. Zhang, T. Wu, D.S. Li, Novel $Zn_{0.8}Cd_{0.2}S@g-C_3N_4$ core-shell heterojunctions with a twin structure for enhanced visible-light-driven photocatalytic hydrogen generation, *J. Mater. Chem. A* 6 (2018) 17086–17094.
- L. Lu, Y. Shen, X. Chen, L. Qian, K. Lu, Ultrahigh strength and high electrical conductivity in copper, *Science* 304 (2004) 422–426.
- M.M. Chen, E. Ma, K.J. Hemker, H. Sheng, Y. Wang, X. Cheng, Deformation twinning in nanocrystalline aluminum, *Science* 300 (2003) 1275–1277.
- B.J. Ng, L.K. Putri, X.Y. Kong, P. Pasbakhsh, S.P. Chai, Overall pure water splitting using one-dimensional P-doped twinned $Zn_{0.5}Cd_{0.5}S_{1-x}$ nanorods via synergetic combination of long-range ordered homojunctions and interstitial S vacancies with prolonged carrier lifetime, *Appl. Catal. B* 262 (2020).
- Y. Yang, C. Zhang, D. Huang, G. Zeng, J. Huang, C. Lai, C. Zhou, W. Wang, H. Guo, W. Xue, R. Deng, M. Cheng, W. Xiong, Boron nitride quantum dots decorated ultrathin porous $g-C_3N_4$: Intensified exciton dissociation and charge transfer for promoting visible-light-driven molecular oxygen activation, *Appl. Catal. B* 245 (2019) 87–99.
- W. Feng, Z. Fang, B. Wang, L. Zhang, Y. Zhang, Y. Yang, M. Huang, S. Weng, P. Liu, Grain boundary engineering in organic-inorganic hybrid semiconductor $ZnS(en)_{0.5}$ for visible-light photocatalytic hydrogen production, *J. Mater. Chem. A* 5 (2017) 1387–1393.
- J. Zhang, J. Yu, M. Jaroniec, J.R. Gong, Noble metal-free reduced graphene oxide- $Zn_xCd_{1-x}S$ nanocomposite with enhanced solar photocatalytic H_2 production performance, *Nano Lett.* 12 (2012) 4584–4589.
- W. Feng, Y. Wang, X. Huang, K. Wang, F. Gao, Y. Zhao, B. Wang, L. Zhang, P. Liu, One-pot construction of 1D/2D $Zn_{1-x}Cd_xS/D-ZnS(en)_{0.5}$ composites with perfect heterojunctions and their superior visible-light-driven photocatalytic H_2 evolution, *Appl. Catal. B* 220 (2018) 324–336.
- Z. Fang, S. Weng, X. Ye, W. Feng, Z. Zheng, M. Lu, S. Lin, X. Fu, P. Liu, Defect engineering and phase junction architecture of wide-bandgap ZnS for conflicting visible light activity in photocatalytic H_2 evolution, *ACS Appl. Mater. Interfaces* 7 (2015) 13915–13924.
- C. Feng, Y. Deng, L. Tang, G. Zeng, J. Wang, J. Yu, Y. Liu, B. Peng, H. Feng, J. Wang, Core-shell $Ag_2CrO_4/N-GQDs@g-C_3N_4$ composites with anti-photocorrosion performance for enhanced full-spectrum-light photocatalytic activities, *Appl. Catal. B* 239 (2018) 525–536.
- J. Shi, S. Li, F. Wang, Y. Li, L. Gao, X. Zhang, J. Lu, In situ topotactic fabrication of direct z-scheme 2D/2D $ZnO/Zn_xCd_{1-x}S$ single crystal nanosheet heterojunction for efficient photocatalytic water splitting, *Catal. Sci. Technol.* 8 (2018) 6458–6467.
- C. Feng, L. Tang, Y. Deng, G. Zeng, J. Wang, Y. Liu, Z. Chen, J. Yu, J. Wang, Enhancing optical absorption and charge transfer: Synthesis of S-doped h-BN with tunable band structures for metal-free visible-light-driven photocatalysis, *Appl. Catal. B* 256 (2019).
- W. Wang, H. Zhang, S. Zhang, Y. Liu, G. Wang, C. Sun, H. Zhao, Potassium ion assisted regeneration of active cyano groups in carbon nitride nanoribbons: visible light driven photocatalytic nitrogen reduction, *J. German Chem. Soc.* 58 (2019) 16644–16650.
- Y. Zhao, R. Shi, X. Bian, C. Zhou, Y. Zhao, S. Zhang, F. Wu, G.I. Waterhouse, L.Z. Wu, C.H.J.A.S. Tung, Ammonia detection methods in photocatalytic and electrocatalytic experiments: how to improve the reliability of NH_3 production

- rates? *Adv. Sci.* 6 (2019) 1802109.
- [37] H. Huang, X.S. Wang, D. Philo, F. Ichihara, H. Song, Y. Li, D. Li, T. Qiu, S. Wang, J. Ye, Toward visible-light-assisted photocatalytic nitrogen fixation: a titanium metal organic framework with functionalized ligands, *Appl. Catal. B* (2020) 118686.
- [38] B. Shao, X. Liu, Z. Liu, G. Zeng, Q. Liang, C. Liang, Y. Cheng, W. Zhang, Y. Liu, S.J.C.E.J. Gong, A novel double Z-scheme photocatalyst $\text{Ag}_3\text{PO}_4/\text{Bi}_2\text{S}_3/\text{Bi}_2\text{O}_3$ with enhanced visible-light photocatalytic performance for antibiotic degradation, *Chem. Eng. J.* 368 (2019) 730–745.
- [39] M. Lashgari, P. Zeinalkhani, Ammonia photosynthesis under ambient conditions using an efficient nanostructured FeS_2/CNT solar-energy-material with water feedstock and nitrogen gas, *Nano Energy* 48 (2018) 361–368.
- [40] Y. Yang, Z. Zeng, C. Zhang, D. Huang, G. Zeng, R. Xiao, C. Lai, C. Zhou, H. Guo, W. Xue, M. Cheng, W. Wang, J. Wang, Construction of iodine vacancy-rich $\text{BiOI}/\text{Ag@AgI}$ Z-scheme heterojunction photocatalysts for visible-light-driven tetracycline degradation: transformation pathways and mechanism insight, *Chem. Eng. J.* 349 (2018) 808–821.
- [41] W. Huang, J. Byun, I. Rörich, C. Ramanan, P.W. Blom, H. Lu, D. Wang, L. Caire da Silva, R. Li, L. Wang, Asymmetric covalent triazine framework for enhanced visible light photoredox catalysis via energy transfer cascade, *J. German Chem. Soc.* 57 (2018) 8316–8320.
- [42] P. Kumar, E. Vahidzadeh, U.K. Thakur, P. Kar, K.M. Alam, A. Goswami, N. Mahdi, K. Cui, G.M. Bernard, V.K. Michaelis, C_3N_5 : a low bandgap semiconductor containing an azo-linked carbon nitride framework for photocatalytic, photovoltaic and adsorbent applications, *J. Am. Chem. Soc.* 141 (2019) 5415–5436.
- [43] G. Zhang, G. Li, Z.A. Lan, L. Lin, A. Savateev, T. Heil, S. Zafeiratos, X. Wang, M. Antonietti, Optimizing optical absorption, exciton dissociation, and charge transfer of a polymeric carbon nitride with ultrahigh solar hydrogen production activity, *Angew. Chem. Int. Ed.* 56 (2017) 13445–13449.
- [44] X. Chen, N. Li, Z. Kong, W.J. Ong, X. Zhao, Photocatalytic fixation of nitrogen to ammonia: state of the art advancements and future prospects, *Mater. Horiz.* 5 (2018) 9–27.